Experimental Study to Enhance Jet Velocity and Power Conversion Efficiency of Piezoelectric Synthetic Jet Actuators

B. Gungordu *
Middle East Technical University, Northern Cyprus Campus, Guzelyurt via Mersin 10, 99738 Kalkanli, Turkey

M. Jabbal† and A. A. Popov‡
University of Nottingham, Nottingham, NG7 2RD, UK

The present work discusses an experimental investigation into the effect of piezoceramic employed to drive a synthetic jet actuator into a quiescent flow. The electromechanical coupling ratio of polycrystalline piezoceramics, PZT-5A/5H, conventionally used in synthetic jet actuators, is inherently low. Therefore, this study aims to investigate using more electromechanically efficient piezoceramics, such as single crystal, PMN-PT. In addition, two different orifice-diaphragm configurations of synthetic jet actuators, opposite and adjacent, are tested. It is identified that PMN-PT piezoceramic promotes three times higher transverse diaphragm displacement and two times more peak jet velocity compared to the PZT-5A piezoelectric actuator for the same input diaphragm voltage. A peak exit jet velocity of 99.5 ms^{-1} was obtained at 40 V of peak supply voltage, which can be classified as a low voltage supply compared to other studies in the literature that obtained similar exit jet velocity. Also, a power conversion efficiency of 72% was achieved, corresponding to the Helmholtz resonance frequency. A new figure-of-merit, momentum coefficient per power consumption, is defined to evaluate the potential impact for full-scale implementation. A state-of-the-art value of 0.09 MW^{-1} is achieved.

Nomenclature

a = speed of sound (ms^{-1})

A_o = orifice area (m^2)

C_μ = momentum coefficient, (%)

d_o = orifice diameter (mm)

d_{31} = transverse piezoelectric coefficient (pm/V)

D = piezoelectric diaphragm diameter (mm)

*Lecturer, Aerospace Engineering, barisgungordu@hotmail.com
†Associate Professor, Aerospace Engineering, mark.jabbal@nottingham.ac.uk
‡Professor, Mechanical Engineering, atanas.popov@nottingham.ac.uk

D_c = cavity diameter (mm)

f_H = Helmholtz resonance frequency (Hz)

f_m = Mechanical resonance frequency (Hz)

E = Young's Modulus (Pa)

E_c = coercive electric field (kV/cm)

h = orifice neck height (mm)

h_{eff} = effective orifice neck height (mm)

H = cavity height (mm)

k_p = electro-mechanical coupling ratio (-)

t_D = total thickness of piezoelectric diaphragm (mm)

T = period of oscillation (s)

P_e = electrical power (W)

P_f = fluidic power (W)

S_v = tail wing area (m^2)

$u(t)$ = instantaneous jet velocity (ms^{-1})

U_p = mean peak velocity (ms^{-1})

U_0 = jet velocity scale (ms^{-1})

V_p = peak supply voltage (V)

V = cavity volume (m^3)

I = current (A)

ν = Poisson's ratio (-)

η = fluidic-to-electric power conversion efficiency (%)

ϕ = phase angle between voltage and current (rad)

ρ = density (kg m^{-3})

ζ = damping ratio (-)

Subscripts

p = peak

rms = root-mean-square

brass = brass substrate

pzt = piezoelectric patch

j = jet

∞ = free-stream conditions

I. Introduction

Synthetic jet actuators (SJA) are zero-net-mass-flux actuators with a wide range of applications, including flow separation and circulation control [1], jet vectoring [2], mixing enhancement [3], and electronic equipment cooling [4]. They present advantages due to their compact size and ease of installation and do not require piping for air supply compared to other active flow control devices. A piezoelectric-driven synthetic jet actuator is a structural, fluidic, and acoustic device that may, in principle, afford improvements in engineering applications, such as providing aerodynamic flow control for drag reduction over an aircraft wing or a vertical tail [5, 6]. SJA has attracted interest in many research work in modelling [7, 8], and experimental [9, 10] in the last two decades.

SJA is driven by a structural or acoustic actuation mechanism, such as a piezoelectric diaphragm, piston, or loudspeaker. Figure 1a presents a schematic of an SJA. The actuation mechanism (here, piezoelectric diaphragm) oscillates periodically to input momentum to the still air in the cavity (air sealed), which then discharges through an orifice turning the flow into an unsteady jet.

The established configuration of the SJA has the arrangement in which the piezoelectric diaphragm is parallel to the orifice (as in Fig. 1a) in which the key sizing parameters of SJA are the cavity diameter (D_c), cavity height (H), orifice diameter (d_o) and orifice neck height (h). In recent years, another configuration, where the diaphragm is adjacent to the orifice, has also been studied (as in Fig. 1b). For a flow control application, SJAs would be used in an array such that actuators are connected in series. The adjacent configuration has the advantage of having closer consecutive orifices, which is important to grant effective flow control. In an array of SJAs, an adjacent design has closer distances between two consecutive orifices, around $\approx O(H)$. For an opposite configuration SJA array, the spacing between consecutive orifice distance is $\approx O(D_c)$, typically 10 to 20 times larger than the adjacent SJA array. Nevertheless, this configuration may promote increased fluidic/pressure losses and reduce jet velocity. In addition, with the adjacent orifice-diaphragm configuration, a higher height (depth) form factor is required, a major constraint in aircraft wing/flap [11].

SJA can be used for various aerodynamic flow control (AFC) settings, including: i) wing flow separation control for fuel savings, ii) nacelle-pylon junction flow instability, which causes lift reduction [12] and, iii) airplane vertical tail, which is oversized to ensure that in case of asymmetric thrust (i.e., engine failure or strong crosswind conditions) sufficient side force can be produced to balance the asymmetry [6]. In case of a successful AFC implementation, the rudder size could be reduced, which would enable a smaller, thus lighter weight vertical tail and reduced drag. Rathay et al. studied slot orifice SJA in small-scale vertical stabilizer models and obtained 20% side force increase at moderate rudder deflection angles [13, 14]. Nevertheless, the performance of the SJA array, such as the peak jet velocity output or the power conversion efficiency, is not reported. However, the peak jet velocity is calculated as 8.2 ms^{-1} with the given parameters, and a momentum coefficient (a measure of jet strength relative to the free-stream air velocity) of 0.248% is obtained. It is also reported that the flow control effectiveness of the SJA decreases with the increasing rudder deflection angle due to the actuators' low momentum transfer; therefore, sweeping jet actuators are nominated for the full-scale

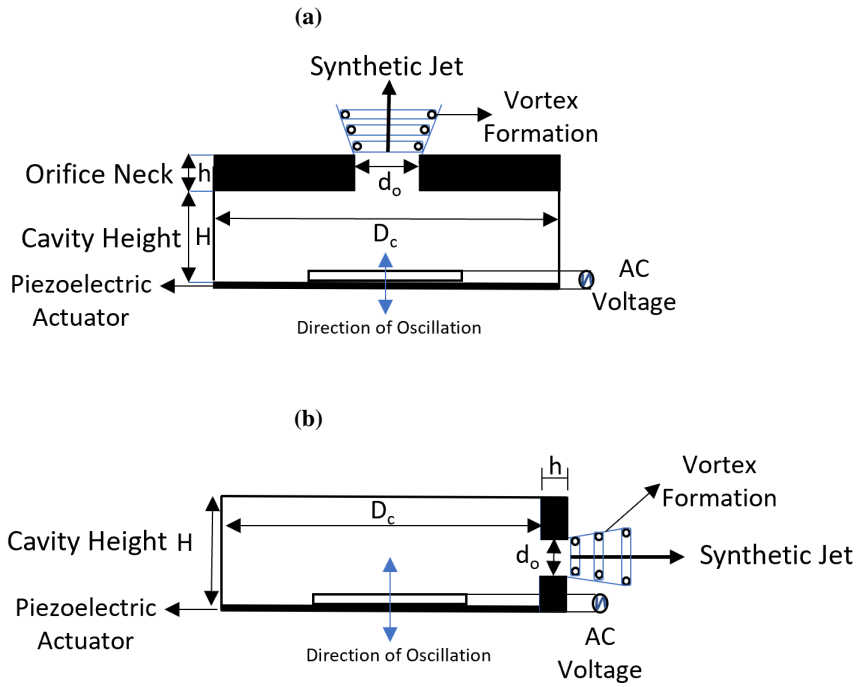

Fig. 1 Schematic of synthetic jet actuator orifice-diaphragm configurations (a) opposite (b) adjacent

flight tests [6]. Hence, further improvement is required on the performance metrics of the SJA.

There has been a wealth of experimental studies on improving the jet velocity and power conversion efficiency of SJA. Gomes and Crowther [9] conducted a parameter sensitivity study to optimise the dimensions of the opposite configuration cavity-orifice arrangement for a 27 mm outer-diameter diaphragm. They obtained a peak exit jet velocity of 130 ms^{-1} with a power efficiency of 7% with a peak supply voltage (V_p) of 125 V_p. Van Buren et al. [15] studied adjacent orifice-diaphragm configuration SJA and obtained an exit jet velocity of 120 ms^{-1} with a power efficiency of 3.5% with a supply voltage of 150 V_p. Recently, Aigouy et al. utilized a piston-based SJA and obtained remarkably high jet velocity with two configurations of relatively large actuators [16]. Nevertheless, the actuator diameter (i.e., characteristic length scale) should be minimized for a potential full-scale aerodynamic flow control application. Table 1 provides a comparison between previously published work and key SJA design parameters (notation consistent with Fig. 1a) and the peak jet velocity (U_p) and power conversion efficiency (η) with corresponding peak supply voltage (V_p).

A circular unimorph piezoelectric diaphragm consists of two main elements: the piezoceramic patch and the metal substrate (here, brass). The elements are bonded together with a thin layer ($\sim$ 10-15 μm) of silver-loaded epoxy to ensure current transfer. SJAs are commonly driven by the polycrystalline piezoceramic family (i.e., PZT-5A, PZT-5H), which inherently has a low electro-mechanical coupling ratio (k_p), thus, not optimal for reduced electrical power consumption.

By inspecting the previous AFC implementation cases of actuators [5, 6, 13, 14] and the performance metrics in the literature (as seen in Table 1), improvements on the SJA performance are required for a potential AFC implementation,

Table 1 Key size, voltage, and performance comparison of the selected experimental SJA research

Study	d_o (mm)	D_c (mm)	V_p (V)	U_p (ms^{-1})	η(%)
[12]	2.5	35	100	100	3
[9]	1.2	25	125	130	7
[15]	1x12	80	150	120	3.5
[15]	1x12	80	150	211	N/A
[17]	1.2	25	45	70	14
[18]	1	27	50	38	15
[19]	2	30.8	100	15	45
[20]	10	52.5	N/A	12	9

especially on power conversion efficiency. A numerical study of Rusovici and Lesieutre on SJA, which is driven by polycrystalline and single crystal piezoelectric actuators, has shown that the single crystal (i.e., PMN-PT) piezoceramic driven SJA, due to the enhanced electromechanical coupling term (k_p), provides a significant enhancement for the power conversion efficiency [21]. As a result, the peak jet velocity of the single crystal SJA was greater than the polycrystalline SJA by about 40%. Nevertheless, the study was not backed-up by an experimental investigation. In addition, Lam et al. studied a single crystal piezoelectric micro-jet with a working fluid of water [22]. The dimensions are quite different than SJA, and the involvement of liquid in the cavity differs from the current study's scope. Lam et al.'s study has shown that, for the same input voltage, the peak displacement of the single crystal ring is 15 times higher than the polycrystalline ring [22]. The results of controlled experiments utilizing common SJA dimensions and piezoelectric diaphragm size composition (i.e., equal diameter and thickness of substrate and piezoceramic) to compare the effects of polycrystalline and single crystal piezoceramic diaphragms on SJA performance are not yet revealed. This paper aims to quantify the effects of employing PZT-5A and PMN-PT-based piezoelectric diaphragms of identical size on SJA performance metrics experimentally through the measurements of diaphragm displacement, exit jet velocity, and electrical power to compute power conversion efficiency. By using two different cavity-orifice configurations, namely opposite and adjacent, the effect of SJA configuration is also to be investigated. The results obtained are then compared with the requirements (i.e., momentum coefficient C_μ, power consumption) of a vertical tail implementation case given by [5]. The manufacturing of the piezoceramic actuators is not included in this study as it is not the research focus of this paper. The piezoelectric elements used within this study can be classified into two groups based on the type of piezoceramic: polycrystalline (here, lead zirconate-titanate, PZT-5A) and single crystal (here, lead magnesium niobate-lead titanate, PMN-PT).

II. Theoretical Background

This section briefly presents the theoretical background of the synthetic jet actuator. It investigates the frequency response, the effects of the piezoceramic characteristic on SJA performance, the computation of the power conversion efficiency, and the sizing of the cavity-orifice arrangements.

A. Frequency Response of SJA

The frequency response of the actuator is usually associated with a double peak response originating from Helmholtz resonance (i.e., cavity acoustic) and mechanical (i.e., diaphragm natural frequency) resonance. SJA is a Helmholtz resonator due to its design, which means it is composed of a closed cavity opened to the exterior via an orifice neck. The fluid inside the cavity acts like a spring, and the orifice neck acts like a mass. The resulting system is a mass-spring oscillator with a natural frequency occurring when reactance reaches zero. The frequency of the Helmholtz resonance highly depends on the actuator geometry, assuming constant fluid density, as shown with Eq. 1.

The frequency response of the SJA (i.e., bi-modal or single-modal) depends on the nonlinear damping factor [23]. For a bi-modal frequency response SJA, the frequency of the first peak is smaller than the cavity acoustic resonance frequency, and the other frequency is greater than the mechanical diaphragm resonance frequency due to the effect of coupling between resonance frequencies [24].

Helmholtz frequency (f_H) for inviscid, incompressible flow is as [7]:

$$f_H = \frac{a}{2\pi}\sqrt{\frac{A_o}{Vh}} = \frac{a}{2\pi}\sqrt{\frac{(d_o/2)^2}{(D_c/2)^2 Hh}} \tag{1}$$

Where a is the speed of sound, A_o is the area of the orifice outlet plane, V is the volume of the cavity, and h is the height of the orifice neck. Eq. 1 does not account for the fluid compressibility effects and heat losses [9], overestimating the Helmholtz resonance frequency. Geometric end corrections of the circular orifice can also be calculated by computing effective orifice neck $h_{eff} = h + 0.85d_0$ [9]. The right-hand side of Equation 1 is for a cylindrical cavity with a circular orifice.

The formula given in Eq. 1 overestimates the Helmholtz frequency by nearly 20%, consistent in various studies [9, 19, 25]. However, whether the overestimation is due to the equation to calculate the Helmholtz resonance or the relative positioning of the Helmholtz resonance with respect to the diaphragm mechanical resonance is not clear.

The mechanical resonance frequency can be estimated using Eq. 2 presented [26]. The equation is also used in a previous SJA study [11].

$$f_m = \frac{4.98 t_D}{2\pi(D/2)^2}\sqrt{\frac{E(1-2\zeta)}{12\rho(1-\nu^2)}} \tag{2}$$

The constant 4.98 is for a simply-supported circular plate, D is the diaphragm diameter, E is the elastic modulus,

ν is the Poisson ratio, t_D is the total diaphragm thickness, ζ is the structural damping. The natural frequency of the composite piezoelectric diaphragm is a function of its dimensions (i.e., diameter and thickness of metal shim and piezoceramic), material properties, and clamping conditions. Therefore, natural frequency estimation in Eq. 2 is not expected to be accurate. De Luca et al. used a similar equation to Eq. 2, which proved to be inaccurate as well [24]. A more detailed study and formulation of the natural frequency of the piezoelectric diaphragm was studied by Prasad et al. [27]. In addition, Yu et al. presented a coupled electro-elastic model for improved accuracy in the estimation of the coupled resonance frequencies [28].

B. Effect of Piezoceramic Characteristic on SJA Performance

SJA performance metrics are the exit jet velocity and device power conversion efficiency. The magnitude of the exit jet velocity is a function of the peak centre diaphragm displacement and the size of cavity-orifice. The peak centre diaphragm displacement (a measure of displaced cavity volume) depends mainly on the transverse piezoelectric coefficient (d_{31}) of the piezoceramic material as the substrate layer does not contribute significantly to the displacement field.

The piezoelectric coupling factor (k_p) indicates the overall electromechanical conversion rate and is a key performance indicator of the PZT-driven SJAs. The piezoelectric coupling factor is always lower than 1 due to the inability of lossless conversion; all of the electrical energy is into mechanical energy and vice versa for the inverse piezoelectric effect. k_p^2 is the ratio between the converted (mechanical) and supplied energy (electrical) and is a measure of the transduction efficiency of the material. The piezoelectric coupling factor (k_p^2) is given by Eq. 3 [29]:

$$k_p^2 = \frac{mechanical\ energy}{electrical\ energy} \tag{3}$$

A special type of piezoceramic is the $Pb(Mg_{1/3}Nb_{2/3})O_3\check{}PbTiO_3$, a high-performance single crystal which is also known as PMN-PT.

PMN-PT has been identified as the next-generation norm piezoceramic with higher electromechanical capabilities [30]. Current drawbacks of PMN-PT are the manufacturing costs and the lower coercive electric field ($E_c \sim 2.0kV/cm$) compared to the PZT family ($E_c \sim 12.0kV/cm$).

C. Power Conversion Efficiency of SJA

The power conversion efficiency (η) is a ratio of fluidic power (P_f) to the electrical power (P_e) expressed by Eq. 4:

$$\eta = \frac{P_f}{P_e} \tag{4}$$

Different definitions regarding the power conversion efficiency of SJA exist in the literature. Table 2 presents the

ambiguity in defining the power conversion efficiency. The phase angle between the voltage and current signal is ϕ, and $\cos(\phi)$ is known as the power factor. To remove the uncertainty in the definition, one should be aware that the power conversion efficiency should be consistent throughout the calculations. If the electrical power is calculated for a whole period of oscillation, the jet velocity should also be calculated for a whole period of oscillation. Even though different notations exist regarding electrical power calculation, there seems to be a technical consistency in the literature. This is because the product integration of the time-dependent voltage and current is equivalent to the root-mean-squares of the phase-matched voltage and current multiplication.

Table 2 Fluidic and electric power definitions of SJA in the literature

Study	Jet Velocity Scale	P_f (W)	P_e (W)
[9, 17]	$U_0^3 = \frac{5}{16}U_p^3$	$\frac{1}{2}\rho A_o U_o^3$	$\frac{1}{T}\int_0^T V(t)I(t)dt$
[15]	$U_0 = \frac{U_p}{\pi}$	$\frac{1}{2}\rho A_o U_0^3$	$\frac{1}{T}\int_0^T V(t)I(t)dt$
[19]	$U_0 = \frac{2U_p}{\pi}$	$\rho A_o U_0^2 c$	$V_{rms}I_{rms}cos(\phi)$
[20]	$U_0 = \frac{U_p}{\pi}$	$\frac{\pi}{3}\rho A_o U_o^3$	$\frac{1}{T}\int_0^T V(t)I(t)dt$
[31]	N/A	$\frac{1}{2}\rho A_o U_p^3$	$\frac{1}{2}V_p I_p cos(\phi + 1)$

For the power conversion efficiency computations in the present study, the approach proposed by Crowther and Gomes [17] is adopted, which stands out as the most representative model. Thus, instantaneous jet velocity, $u(t)$, is modelled with Eq. 5 using an expression for a biased sinusoid with the peak velocity (U_p), and it fits well to 1-D jet velocity measurement:

$$u(t) = \frac{U_p}{2}(1 - \cos(\omega t)) \tag{5}$$

The fluidic power (P_f) over a cycle is then given by Eq. 6:

$$P_f = \frac{1}{2}\rho A_o u(t)^3 = \frac{1}{2}\rho A_o (\frac{1}{T}\int_0^T u(t)^3) = \frac{1}{2}\rho A_o (\frac{5}{16}U_p^3) \tag{6}$$

D. Sizing of Cavity-Orifice Arrangement

The opposite orifice-diaphragm configuration SJA dimensions are consistent with the jet velocity optimized design of Gomes et al., which is identified as a result of a comprehensive sensitivity analysis [9]. It is a known SJA design feature where the cavity height is inversely proportional to the jet velocity [32, 33]. A shallower cavity promotes a larger jet velocity due to the increased swept volume of the diaphragm compared to the volume of the cavity. Also, a stronger vortex pair forms in the case of a shallow cavity design [33]. The ratio of the cavity height to the cavity diameter is 0.027, and the design can be classified as a pancake shape SJA (i.e., $H/D_c < 0.5$).

The adjacent orifice-diaphragm SJA has an increased pressure loss term due to the bending of the flow during the

discharge (ejection) phase, which is likely to result in reduced jet velocity compared to the opposite configuration SJA. Also, the smaller net cavity volume change in this configuration can explain the increased pressure loss. Additionally, there is a design constraint: the cavity height must be larger than the orifice diameter, H > d_o. Therefore, the cavity height (H) has to increase compared to the opposite orifice-diaphragm configuration SJA. The orifice diameter is reduced to 1.0 mm to minimize the cavity height and to increase the jet velocity. The orifice neck length is kept constant to be consistent with the opposite configuration SJA.

III. Methodology

This section presents the physical properties of the piezoelectric actuators, the manufacturing of cavity-orifice arrangements, and experimental methods for measuring the diaphragm displacement, jet velocity, and electrical power measurements.

A. Piezoelectric Actuators

Unimorph polycrystalline and single-crystal piezoelectric diaphragms are supplied by OBO Pro2 Inc. and TRS Ceramics, respectively. Table 3 presents the size and thickness compositions of the polycrystalline (PZT-5A) and single crystal (PMN-PT) piezoceramic actuators and their piezoelectric properties. The material properties are provided by the manufacturers of the piezoelectric actuators. Based on the coercive electric field and piezoceramic thickness, the maximum supply voltage of the single crystal diaphragm is 45 V_p. This limits the experimental investigation herein to 40 V_p, which is the supply voltage single crystal diaphragm that can hold without experiencing failure. Table 3 also presents the material properties of the PZT-5A and PMN-PT diaphragms.

Table 3 Polycrystalline and single crystal actuator dimensions and properties

Parameter	PZT-5A	PMN-PT
D_{brass} (mm)	27	27
D_{pzt} (mm)	19.8	19.8
t_{brass} (mm)	0.22	0.22
t_{pzt} (mm)	0.23	0.23
d_{31} (pm/V)	-180	-560
d_{33} (pm/V)	375	1200
k_p (-)	0.4	0.9
E_c (kV/cm)	12.0	2.0
Brass - ρ (kg/m^3)	8500	8450
Brass - E (Pa)	110	103
Brass - ν (-)	0.34	0.33
Piezoceramic - ρ (kg/m^3)	7500	8100
Piezoceramic - E (Pa)	60	115
Piezoceramic - ν (-)	0.32	0.32

B. Cavity-Orifice Arrangement Manufacturing

The opposite and adjacent configuration SJA arrangements are printed with Stereolithography (SLA) Printer (Formlabs Form 2), which can provide a precise print dimension. A grey hard pro resin material is used. The size precision of the product is 0.05 mm. The prints are washed, cured, and polished to ensure a smooth surface finish.

Figure 2 presents an exploded view of the cavity-orifice arrangement and the piezoelectric diaphragm. The figure presents the view from the inner side of the cavity and shows the brass substrate, cavity depth with the orifice, piezoelectric element, and outer side of the clamping plate.

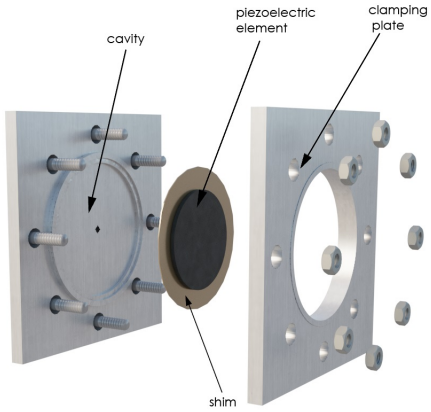

Fig. 2 3-D assembly drawing of the opposite cavity-orifice arrangement and piezoelectric diaphragm

The dimensions of the cavity-orifice size and the diaphragms are presented in Table 4. The notation used in the table is consistent with Figure 1a.

Table 4 Cavity-orifice arrangement size of opposite and adjacent SJA configurations

Parameter	Opposite	Adjacent
d_o (mm)	1.2	1.0
D_c (mm)	25	25
h (mm)	2.5	2.5
H (mm)	0.67	1.2

C. Experimental Methods

The cavity-acoustic and mechanical resonance frequencies, computed by Equation 1 and Equation 2 respectively, are 1700 Hz and 2070 Hz. Thus, the frequency sweeps are conducted in the range of 100 Hz to 4000 Hz to cover both predicted resonances well beyond the mechanical resonance frequency. Frequency sweep is conducted with 100 Hz increments, but for better frequency resolution near the peak frequencies, an increment of 50 Hz was employed. The voltage sweeps are limited to 20 V_p, 30 V_p, and 40 V_p.

The actuator excitation signal was generated using an SR785 (Stanford Research) signal generator. Sinusoidal excitation was used for all the tests conducted. The signal was amplified using a Trek Piezo Driver/Power Amplifier Model PZD350. This amplifier provides monitor channels for low-voltage representation of the high-voltage output and current sensing for power measurement. The real-time data acquired using an analog-to-digital converter (NI cDAQ-9171) is connected to the computer (i.e., data acquisition software).

1. Diaphragm Displacement Measurements

The centre position of the circular diaphragm is targeted as it is one of the key piezoelectric performance indicators and is linked to the exit jet velocity in many studies [34, 35].

The diaphragm is placed in the groove-lip arrangement of the actuator, which is supported by uniform clamping. The laser scanning head used is a PSV-300 (Polytec). The laser measurements identify the resonant frequency and peak displacement at the centre of the diaphragm. The laser controller was integrated into a dynamic signal generator and analyzer (SR 785). Displacement measurements are taken in mm/s/V, then integrated with post-processing to obtain the peak displacement.

The measurements are taken with a sampling rate of 40 kHz, which grant the Nyquist sampling criteria since the maximum actuation frequency is 4 kHz [36]. The resolution of the measurements is 5 $\mu m/s$. The displacement amplitude error at room temperature is ±1.5% of the root-mean-square of the reading.

2. Power Measurements

Simultaneous and real-time acquisition of voltage and current are required to calculate the power consumption of the SJA. Electrical power is the product of voltage and current. For alternating current systems, the true power (also referred to as actual power) is calculated by also taking into account the phase difference between the voltage and current signals.

The sampling rate is 40 kHz for both voltage and current signals. The sampling time is 10 seconds, which results in a sample size of 400,000 for each actuation frequency. Measurements for electrical power are taken simultaneously with jet velocity. The voltage and current measurements have an uncertainty of ± 0.1% and ± 1%, respectively.

3. Jet Velocity Measurements

Hot-wire anemometry (HWA), MiniCTA 54T30 (Dantec Dynamics), is used for the jet velocity measurements with a 55P11 probe. The probe is positioned in line with the orifice centre-line throughout the experiments. Dantec 55P11 probe consists of a platinum-plated tungsten wire with a width of 1.2 mm (which is equal to or smaller than d_o) and a diameter of 5 μm.

Figure 3 illustrates the HWA setup. In the horizontal axis, the probe is placed as close as possible to the exit plane to sample the maximum possible jet velocity corresponding to a downstream distance of 0.1 d_o. The approach is identical

to the experimental work of Gallas et al. [37] and Persoons [38]. The probe's position is manually set using a digital vernier caliper with a ±0.05 mm resolution.

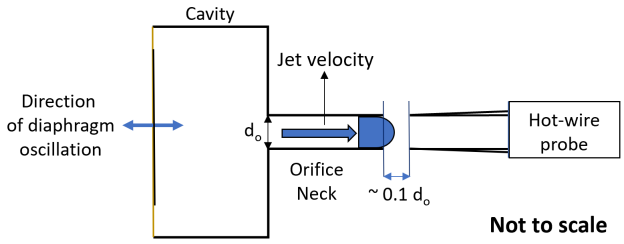

Fig. 3 Illustration of hot-wire probe positioning and setup

Hot-wire calibration uses a nozzle rig, standard K-type thermocouples to measure flow temperature, and a Furness Control FC0510 micro-manometer. The hot-wire probe is calibrated up to a 150 ms^{-1} velocity, and the calibration curve is fitted to a 5^{th} order polynomial. The sampling frequency and sample size are 10 kHz (satisfies Nyquist sampling criteria) and 100,000 for each forcing frequency. The measurements are corrected for temperature drift. The equipment accuracy of the hot-wire system and the calibration and positioning error is 3%.

IV. Results and Discussion

This section presents the experimental results for the measurements of centre diaphragm displacement, exit jet velocity, current consumption, and computation of power conversion efficiency for opposite and adjacent cavity-orifice configurations for each diaphragm, PZT-5A, and PMN-PT. The diaphragm displacement is presented separately, as it is common for both actuator configurations. Figures reflect the frequency and voltage sweeps for all measurements in a single plot.

A. Diaphragm Displacement

The mean peak centre diaphragm displacement measurements are presented in this section. The displacement of the diaphragm is proportional to the jet velocity; therefore, it is an important indication of piezoelectric actuator performance. Figure 4a presents the voltage sweep over the forcing frequency range of the PZT-5A diaphragm. The mechanical resonance frequency is 2950 Hz. The peak displacement at the resonant frequency is 15.8 μm, 24.1 μm and 32.2 μm for 20 V_p, 30 V_p and 40 V_p, respectively. Figure 4b presents the voltage sweep over the forcing frequency range of the PMN-PT diaphragm. The mechanical resonance frequency is 2800 Hz. The increased diaphragm displacement at the Helmholtz resonance (1500 Hz) is also observed. The peak displacements at the resonant frequency are 47.9 μm, 60.5 μm and 82.7 μm for 20 V_p, 30 V_p and 40 V_p, respectively. It is observed that the PMN-PT diaphragm yields approximately three times more peak centre displacement than the PZT-5A diaphragm.

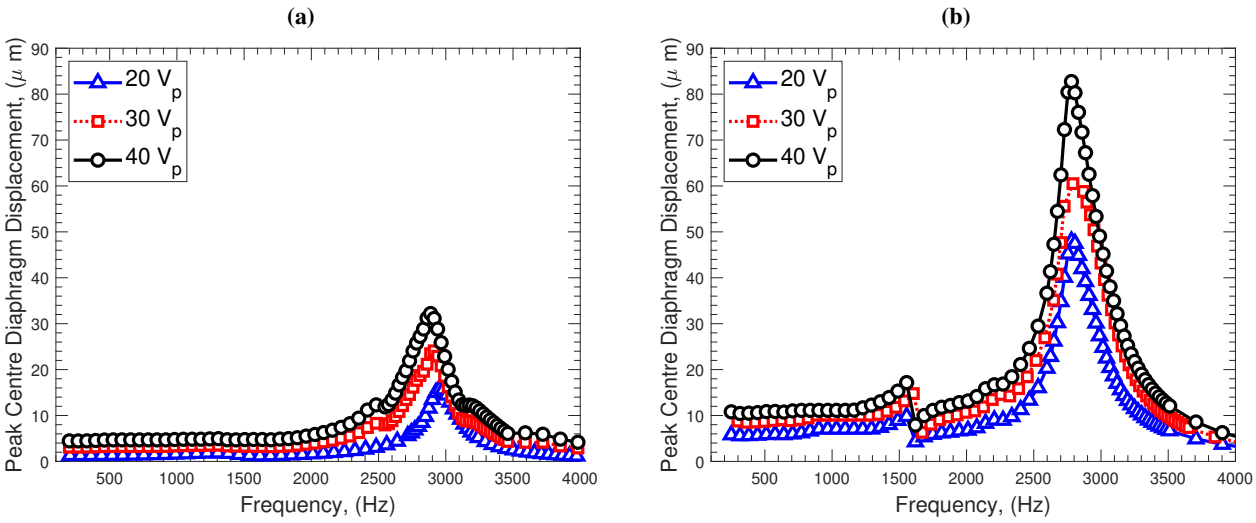

Fig. 4 Centre peak diaphragm displacements of SJA (a) PZT-5A diaphragm driven SJA (b) PMN-PT diaphragm driven SJA

B. Opposite Orifice-Diaphragm Configuration

1. Jet Velocity

Figure 5a presents the jet velocity measurements of the PZT-5A diaphragm. Due to the cavity acoustic and diaphragm mechanical resonance, the double peak occurrence is observed for all three supply voltages. The first resonance peak is associated with the cavity-acoustic resonance, and the second resonance is due to the diaphragm mechanical frequency.

The jet velocities corresponding to the cavity acoustic and diaphragm mechanical resonance increase with the supply voltage. The jet velocities corresponding to the cavity acoustic resonance of the PZT-5A diaphragm are 20.1 ms^{-1}, 26.0 ms^{-1} and 34.0 ms^{-1} for 20 V$_p$, 30 V$_p$, and 40 V$_p$, respectively. The mean peak jet velocities corresponding to the mechanical resonance are 36.8 ms^{-1}, 49.9 ms^{-1} and 65.0 ms^{-1} for 20 V$_p$, 30 V$_p$, and 40 V$_p$, respectively.

Figure 5b presents the jet velocity measurements of the PMN-PT diaphragm. The jet velocities corresponding to the cavity acoustic resonance of the PMN-PT diaphragm are 45.0 ms^{-1}, 55.6 ms^{-1} and 64.4 ms^{-1} for 20 V$_p$, 30 V$_p$, and 40 V$_p$, respectively. The mean peak jet velocities corresponding to the mechanical resonance are 70.7 ms^{-1}, 86.1 ms^{-1} and 99.5 ms^{-1} for 20 V$_p$, 30 V$_p$, and 40 V$_p$, respectively. The jet velocity of the PMN-PT diaphragm-driven SJA is two times more than the PZT-5A with a supply voltage of 20 V$_p$, but the amplification decreases with increasing voltage. On the other hand, the exit jet velocity corresponding to the cavity acoustic resonance of the PMN-PT actuator is approximately equal to the mechanical resonance jet velocities of the PZT-5A diaphragm.

The fluidic/pressure losses scale with U_p^2; therefore, the increase of jet velocity with voltage is non-linear. The potential reasons for this are the compressibility effects, voltage-dependent piezoceramic saturation/dissipation, and the increased pressure loading acting on the diaphragm. The cavity acoustic resonance increases with the voltage linearly in

both cases, whereas the viscous and compressibility effects are less.

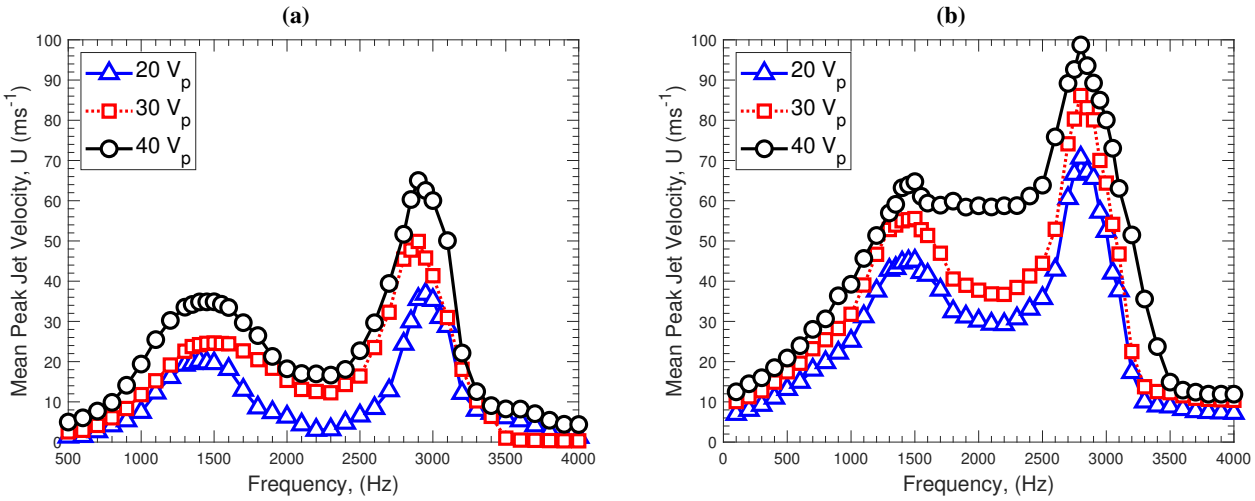

Fig. 5 Opposite configuration SJA - mean peak exit jet velocity (a) PZT-5A diaphragm driven SJA (b) PMN-PT diaphragm driven SJA

2. Current Draw

Figure 6a presents the current drawn by the PZT-5A diaphragm actuator. The peak currents of the PZT-5A diaphragm are 11.2 mA, 14.4 mA, and 20 mA for supply voltages of 20 V_p, 30 V_p, and 40 V_p, respectively.

Figure 6b presents the current drawn by the PMN-PT diaphragm-driven SJA. It is identified that the PMN-PT diaphragm consumes approximately twice as much of the current drawn by the PZT-5A diaphragm. The PMN-PT diaphragm has a peak current consumption of 24.4 mA, 36 mA, and 45.9 mA for supply voltages of 20 V_p, 30 V_p, and 40 V_p, respectively. The peak current consumption coincides with the resonant frequency for both diaphragms.

It should be noted that the peak current drawn by the PMN-PT diaphragm shifts -100 Hz at 40 V_p with the resonant peak. The peak frequency shifts are observed in nonlinear SJA systems as the driven voltage increases [39]. In addition, this change may also be due to the increased displaced volume in the cavity, which changes the relative positions of cavity acoustic and diaphragm mechanical resonance.

3. Power Conversion Efficiency

Figure 7a presents the power conversion efficiency of the PZT-5A diaphragm. The peak power conversion efficiency is identified at the cavity acoustic resonance, which has relatively high jet velocity and low current consumption. The power conversion efficiencies at the mechanical resonance frequency are 15.9%, 13.4% and 9.4% corresponding to the supply voltages of 20 V_p, 30 V_p and 40 V_p, respectively. At 20 V_p, cavity acoustic and diaphragm mechanical resonances' power conversion efficiency is approximately equal. The increasing voltage decreases the efficiency around the diaphragm mechanical resonance and increases near the actuation frequencies around the cavity acoustic resonance.

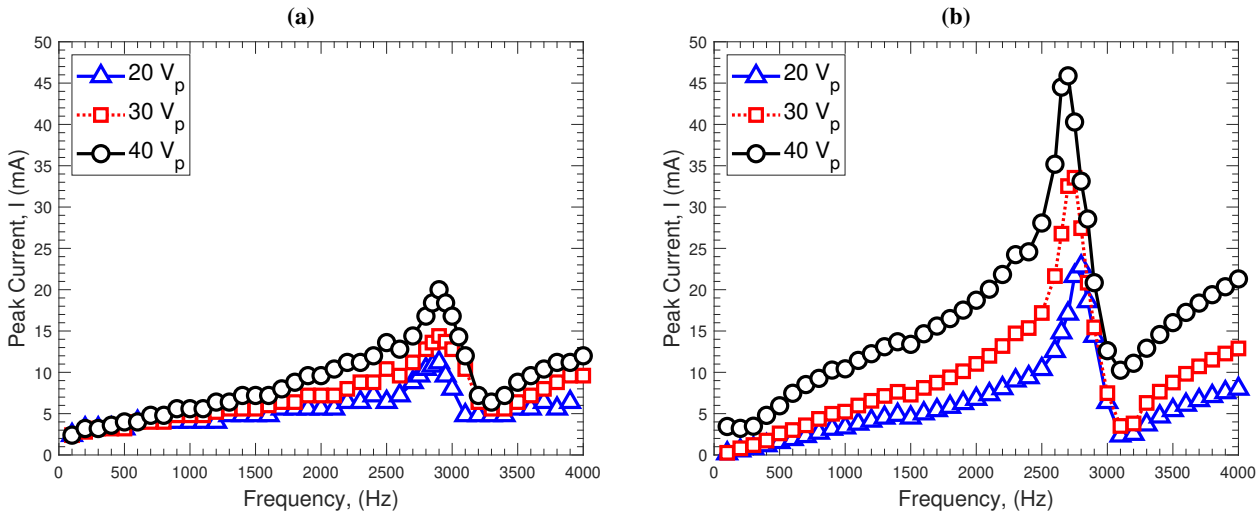

Fig. 6 Opposite configuration SJA - mean peak current draw (a) PZT-5A diaphragm driven SJA(b) PMN-PT diaphragm driven SJA

This is thought to be due to more dominant compressibility effects and fluidic losses, which limit the jet velocity and increase both voltage supply and current draw.

Figure 7b presents the power conversion efficiency of the PMN-PT diaphragm. The power conversion efficiencies at the mechanical resonance frequency are 39.5%, 30.7%, and 23.0% corresponding to the supply voltages of 20 V_p, 30 V_p and 40 V_p, respectively. The power conversion efficiency at the mechanical resonance and neighboring frequencies reduces with the increasing supply voltage.

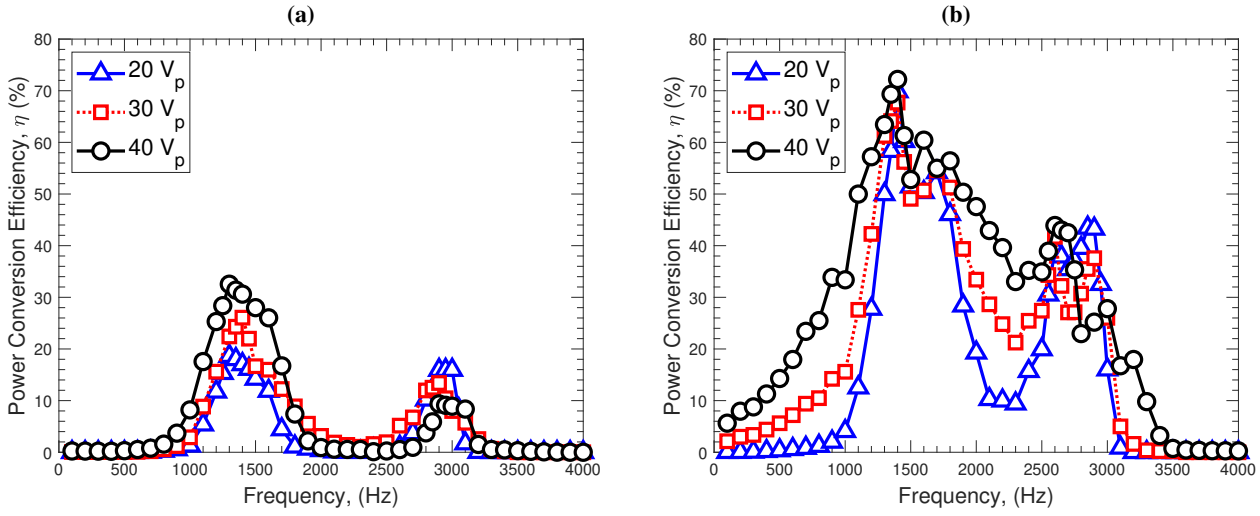

Fig. 7 Opposite configuration SJA - power conversion efficiency (a) PZT-5A diaphragm driven SJA (b) PMN-PT diaphragm driven SJA

At the actuation frequency around the mechanical resonance, the power conversion efficiency is bimodal due to the double peak occurrence of the power factor (cosϕ) shown in Figure 8.

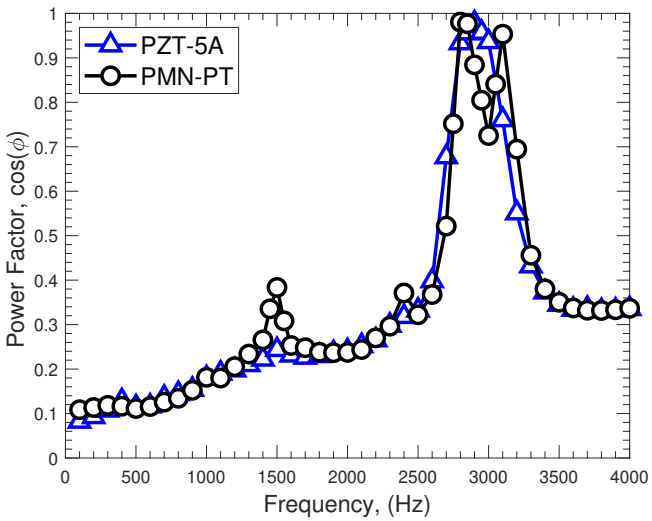

Fig. 8 Power factor (cos ϕ) of PZT-5A and PMN-PT diaphragms

Frequencies around the cavity acoustic resonance promote an increased jet velocity with a relatively lower current consumption increase compared to the mechanical resonance frequency. Therefore, the efficiency is conserved with increasing voltage. It is observed that the power conversion efficiency and the voltage supply are inversely proportional in the middle region between the two resonance peaks. This is due to the low jet velocity and high current consumption at 20 V_p, which then alternate because of lower current increment and a higher jet velocity with the increasing supply voltage.

When the power conversion efficiency of the PZT-5A and PMN-PT-driven SJA is compared, it is observed that the cavity-acoustic resonance-dominated region promotes the largest power conversion efficiency in both cases. PMN-PT diaphragm promotes approximately a threefold increase in power conversion efficiency across all supply voltages when comparing peak efficiency ratios.

Table 5 presents the peak power conversion efficiency and corresponding peak exit jet velocity for both diaphragm types. The table contains power conversion efficiency (η) and peak exit jet velocity (U_p). Regardless of the supply voltage, peak conversion efficiency and peak jet velocity are presented. The peak efficiency for the PZT-5A and PMN-PT are presented with their corresponding jet velocity and vice versa.

Table 5 Opposite Configuration SJA - Comparison of peak power conversion efficiency values

	PZT-5A		PMN-PT	
	η (%)	U_p (ms^{-1})	η (%)	U_p (ms^{-1})
Peak Efficiency	33.2	33.5	72.2	63.2
Peak Jet Velocity	16	65.1	23	99.5

C. Adjacent Orifice-Diaphragm Configuration

1. Jet Velocity

Figure 9a presents the mean peak jet velocity results of PZT-5A diaphragm for 20 V_p, 30 V_p and 40 V_p of the supply voltage. It is observed that the cavity acoustic resonance is located at 900 Hz, and the diaphragm mechanical resonance is identified at 2900 Hz. The exit jet velocities corresponding to the cavity acoustic resonance are 16.7 ms^{-1}, 24.9 ms^{-1}, and 32.9 ms^{-1}. The peak jet velocities at the diaphragm mechanical resonance are 33.8 ms^{-1}, 46.1 ms^{-1} and 58.3 ms^{-1} for 20 V_p, 30 V_p, and 40 V_p, respectively.

Figure 9b presents the mean peak jet velocity results of PMN-PT diaphragm for 20 V_p, 30 V_p, and 40 V_p of the supply voltage. It is observed that the cavity acoustic resonance is also located at 900 Hz, and the diaphragm mechanical resonance is identified at 2800 Hz. The exit jet velocities corresponding to the cavity acoustic resonance are 31.1 ms^{-1}, 40.0 ms^{-1}, and 52.5 ms^{-1}. The peak jet velocities at the diaphragm mechanical resonance are 61.9 ms^{-1}, 74.2 ms^{-1} and 90.3 ms^{-1} for 20 V_p, 30 V_p, and 40 V_p, respectively.

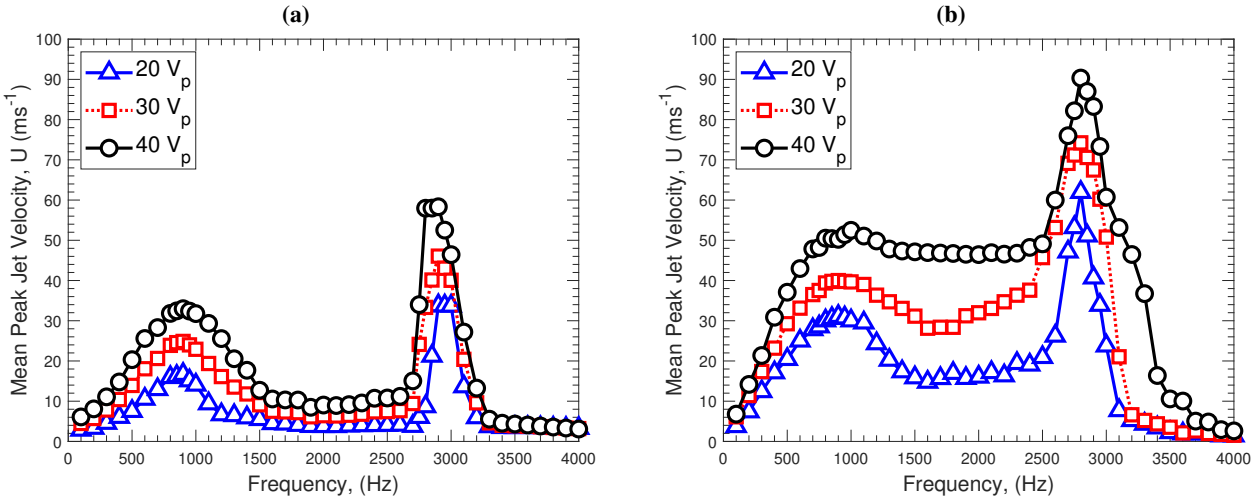

Fig. 9 Adjacent configuration SJA - mean peak exit jet velocity (a) PZT-5A diaphragm driven SJA (b) PMN-PT diaphragm driven SJA

PMN-PT diaphragm promotes 2 times more jet vet velocity at 20 V_p, reducing the ratio to 1.5 times at 40 V_p. The adjacent SJA reduced jet velocity for both diaphragm types compared to the opposite configuration SJA.

2. Current Draw

Figure 10a presents the current drawn by the PZT-5A diaphragm-driven actuator. It is identified that the PMN-PT diaphragm consumes approximately twice as much of the current drawn by the PZT-5A diaphragm. The peak currents of the PZT-5A diaphragm are 13.6 mA, 15.6 mA, and 21.3 mA for supply voltages of 20 V_p, 30 V_p, and 40 V_p, respectively. Figure 10b presents the current drawn by the PMN-PT diaphragm actuator. The PMN-PT diaphragm has a

peak current consumption of 25.1 mA, 40 mA, 51.2 mA for supply voltages of 20 V_p, 30 V_p, and 40 V_p, respectively. The peak current consumption coincides with the resonant frequency for both diaphragms. It is observed that the current consumption has increased by around 10% for the adjacent SJA compared to the opposite SJA. This is thought to be a result of the increased pressure loading on the disc due to the reduced volume of the cavity and less fluid discharge due to the adjacent orifice-diaphragm configuration.

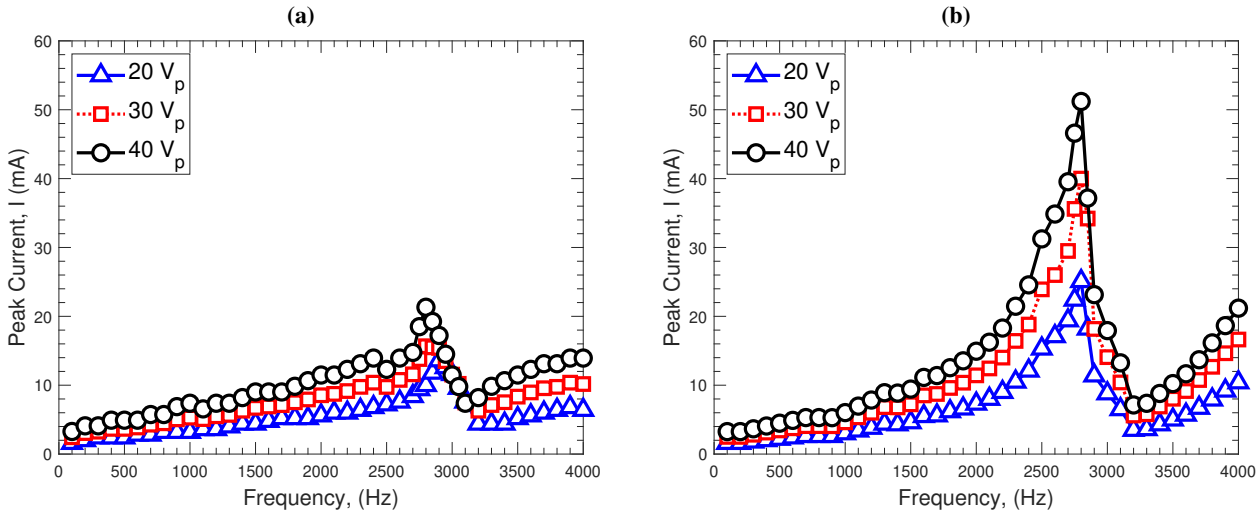

Fig. 10 Adjacent configuration SJA - mean peak current draw (a) PZT-5a diaphragm driven SJA (b) PMN-PT diaphragm driven SJA

3. Power Conversion Efficiency

Figure 11a presents the power conversion efficiency for the PZT-5A diaphragm. The power conversion efficiencies at the mechanical resonance frequency are 8.0%, 12.8% and 17.6% corresponding to the supply voltages of 20 V_p, 30 V_p and 40 V_p, respectively. The power conversion efficiency increases with increasing supply voltage at the mechanical resonance and neighboring frequencies. This trend is similar to the result of the opposite SJA. The efficiency corresponding to the cavity acoustic resonance has increased compared to the opposite configuration due to cavity acoustic resonance taking place on a lower forcing frequency with less current consumption.

Figure 11b presents the power conversion efficiency for the PMN-PT diaphragm. The power conversion efficiencies at the mechanical resonance frequency are 38.0%, 28.6% and 19.2% corresponding to the supply voltages of 20 V_p, 30 V_p and 40 V_p, respectively. The trend between the efficiency and voltage at the mechanical resonance is similar to the opposite SJA. The peak efficiency values at the mechanical resonance frequency are reduced with increasing voltage due to the additional pressure losses prescribed by the adjacent configuration. Also, with the incremental voltage, the jet velocity increase is insufficient to preserve the conversion efficiency rate. In addition, the power conversion efficiency decrease is due to the orifice diameter reduction in adjacent SJA compared to the opposite SJA (from 1.2 mm to 1.0

mm). The jet velocity at the surrounding frequencies of the cavity acoustic resonance promotes an increased jet velocity as the supply voltage increases with a relatively lower increase of the current consumption (compared to the current consumption increase in mechanical resonance frequency). Therefore, the efficiency is conserved with the increasing voltage.

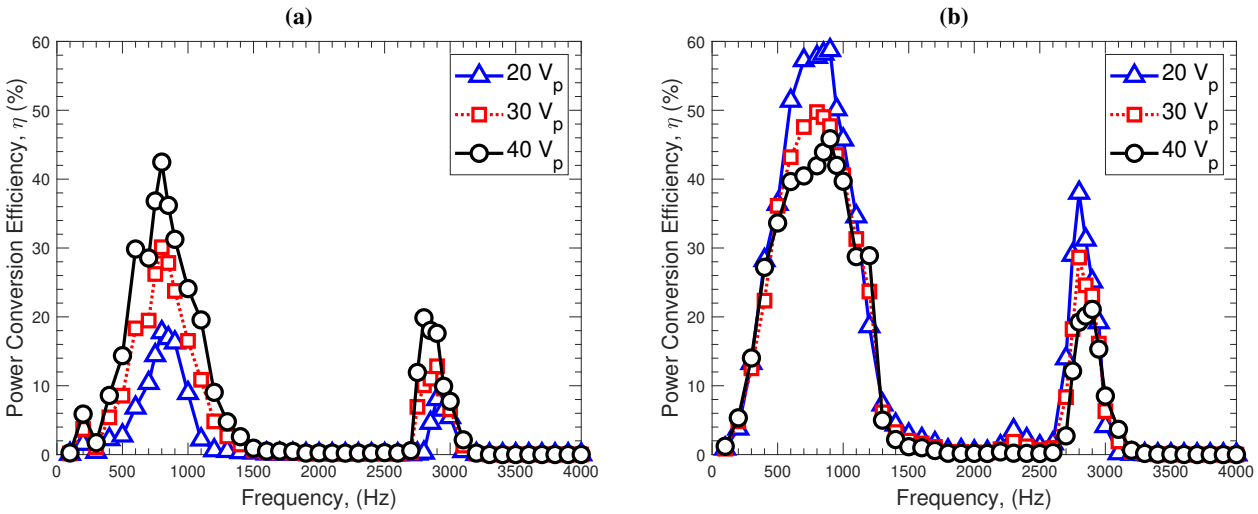

Fig. 11 Adjacent configuration SJA - power conversion efficiency (a) PZT-5A diaphragm driven SJA (b) PMN-PT diaphragm driven SJA

Table 6 presents both diaphragm types' peak power conversion efficiency and corresponding jet velocity. It should be noted that the peak jet velocity and peak power conversion efficiency do not occur at the same actuation frequency. The table presents peak conversion efficiency and peak jet velocity regardless of the supply voltage.

Table 6 Adjacent configuration SJA - Comparison of peak power conversion efficiency values

	PZT-5A		PMN-PT	
	η (%)	U_p (ms^{-1})	η (%)	U_p (ms^{-1})
Peak Efficiency	42.5	31.8	58.7	31.1
Peak Jet Velocity	19.9	58.0	19.2	90.3

V. Implications for Full-Scale Application

This section presents the potential impact of the PMN-PT-driven SJA configurations studied herein at the aircraft system level. Mooney et al. conducted an AFC study to evaluate the potential benefits of reducing the size of aircraft vertical tail. They established the requirements of the candidate flow control mechanisms, including synthetic jet actuator [5]. The principal functional requirements are named as momentum coefficient (C_μ) and electrical power consumption. The authors [5] evaluated the ratio of the average jet velocity of the synthetic jet and free-stream by using

a non-dimensional momentum coefficient, which reads as:

$$C_\mu = \frac{2\rho_j n A_o U_j^2}{\rho_\infty U_\infty^2 S_v} \tag{7}$$

An acceptable value of C_μ to grant effective flow control is suggested to be 0.5% for the jet velocity of the actuator for such flow control application [5]. They assumed a free-stream condition of 130 knots (i.e., U_∞ = 67 ms^{-1}) and a tail wing area of 470 ft^2 (i.e., S_v = 43.7 m^2). The required number of actuators (n) is given as 200. The air density terms can be neglected, and the jet velocity term (U_j) is linked to the peak jet velocity by $U_j = 2\pi U_p/3$ [5]. On the other hand, the electrical power (P_e) required for the AFC should be limited to 450 kW due to the capability of auxiliary power units [5]. Thus, it could be suggested that the enhanced exit jet velocity of the actuator is equally important to achieve low power consumption (i.e., high power conversion efficiency).

As seen in Table 1, the highest jet velocity and the highest power conversion efficiencies are reported by Van Buren et al. [15], and by Feero et al. [19], respectively. They were used to compare the results obtained in the present study. With the given limitation of the auxiliary power unit, Van Buren et al. configuration can support a maximum of 46 actuators, while Feero et al. configuration can support 1390 actuators. The PMN-PT-driven SJA of the present study can support 200 actuators.

The required momentum coefficient and the power supply limit can be divided to establish a new figure of merit and gain insight into the potential full-scale implementation. Figure 12 presents a ratio of C_μ to P_e for 200 actuators to satisfy the power supply requirement for 60 minutes of continuous operation. Three studies: Van Buren et al. [15], Feero et al. [19], and the present study, are compared. The present study is represented by the performance of PMN-PT-driven SJAs at the highest jet velocity with 40 V_p supply voltage.

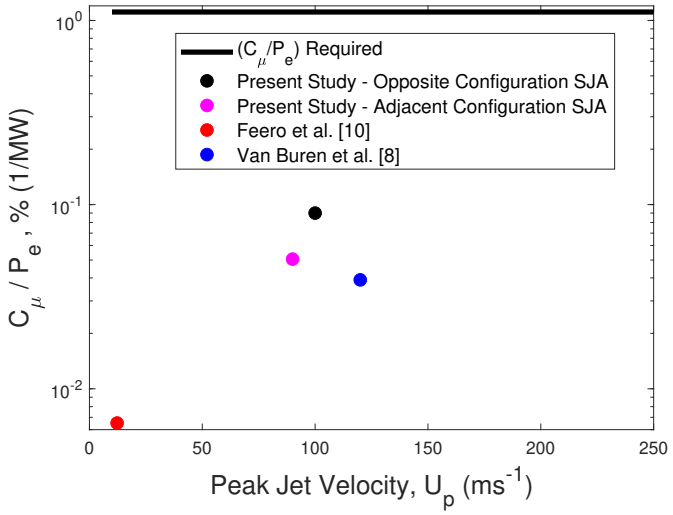

Fig. 12 C_μ/P_e calculations for the conditions provided by Mooney et al. [5]

By the calculation presented in Figure 12, it is identified that the momentum coefficient per the power consumed of the current study is evidently the most state-of-the-art value reported to date. Table 7 presents the number of actuators the investigated studies can support for 60 minutes of continuous operation with 450 kW of power supply. Compared to Van Buren et al. [15], the momentum coefficient per the power consumption is improved by 130% and 30% with opposite and adjacent configuration SJA, respectively. In addition, the target number of actuators realized in the present study satisfies 200 actuators.

Table 7 Number of actuators that can support 60 minutes of continuous operation for 450 kW power supply

Study	Number of SJA
Feero et al. [19]	1390
Van Buren et al. [40]	46
Present study - Opposite SJA	200
Present study - Adjacent SJA	176

VI. Conclusions

The experimental campaign using the single crystal-driven SJA has proven that a peak jet velocity of approximately 100 ms^{-1} and efficiency of 40% can be achieved, which stands out as a significant improvement in the field, compared to the cases listed in Table 1.

It is also demonstrated that changing the SJA configuration from opposite to adjacent orifice-diaphragm reduces the peak jet velocity by around 10% due to two causes. Firstly, the cavity height used in the adjacent orifice-diaphragm configuration is around two times higher than that used in the opposite configuration SJA. Secondly, due to the bending of the flow during the ejection cycle, the pressure losses are increased in the adjacent configuration. Maintaining short spacing between two adjacent orifices is important to grant effective flow control. The results presented in this study are particularly important for the potential applications as the spacing between adjacent orifices can be reduced without a significant jet velocity reduction.

The key findings and conclusions of the study are listed below.

(1) The peak centre diaphragm displacement of the PMN-PT diaphragm-driven SJA is three times larger than the identical size PZT-5A diaphragm across all supply voltages (i.e., 20-30-40 V_p).

(2) The peak jet velocity exhibits a twofold increase (37 ms^{-1} to 71 ms^{-1}) when a single crystal diaphragm is employed at 20 V_p of the supply voltage. With 40 V_p, a jet velocity of 99.5 ms^{-1} is achieved by the PMN-PT diaphragm SJA, compared to the 65 ms^{-1} produced by the PZT-5A diaphragm SJA.

(3) The current consumption peaks around the mechanical resonance frequency for both diaphragm types and increases proportionally with the supply voltage. The peak current consumption of the PMN-PT SJA is twice as high as

that of the PZT-5A diaphragm SJA.

(4) The power conversion efficiency tends to be larger at around cavity acoustic resonance frequency than the mechanical resonance for both diaphragms. A peak power conversion efficiency of 72.2% is achieved with the PMN-PT diaphragm, corresponding to a jet velocity of 63.2 ms^{-1}. Also, a power conversion efficiency of 23% is achieved, corresponding to a jet velocity of 99.5 ms^{-1}, which is a twofold increase of the power conversion efficiency compared to the PZT-5A diaphragm. The time-dependent behavior of the voltage and current signals revealed that the capacitive nature of the diaphragm tends to be reactive at the mechanical resonance frequency; power factor $\cos(\phi)$ tends to be 1.

(5) The adjacent orifice-diaphragm configuration SJA has a reduced peak jet velocity of approximately 10% for both diaphragm types across all voltages, compared with the opposite configuration SJA. The peak jet velocity with the PMN-PT diaphragm is 90 ms^{-1} at a supply voltage of 40 V_p. A peak power conversion efficiency of 51.2% is achieved with the PMN-PT diaphragm corresponding to a jet velocity of 52.5 ms^{-1}.

(6) A new parameter, momentum coefficient per the power consumption, which is beneficial as a measure for potential full-scale implementation, is defined, and the state-of-the-art value (0.09 MW^{-1}) is established in this study, which is a 130% improvement compared to the previously reported studies.

References

[1] Itsariyapinyo, P., and Sharma, R. N., "Experimental Study of a NACA0015 Circulation Control Airfoil Using Synthetic Jet Actuation," *AIAA Journal*, Vol. 60, No. 3, 2022, pp. 1612–1629. https://doi.org/10.2514/1.J060508, URL https://doi.org/10.2514/1.J060508.

[2] Jiang, S., Yu, J., Yin, S., Yang, Y., Chen, F., and Sullivan, P. E., "Uncertainty quantification of separation control with synthetic jet actuator over a NACA0025 airfoil," *Aerospace Science and Technology*, Vol. 133, 2023, p. 108106. https://doi.org/10.1016/j.ast.2023.108106, URL https://doi.org/10.1016/j.ast.2023.108106.

[3] Ja'Fari, M., Jaworski, A. J., and Rona, A., "Numerical study of flow separation control over a circular hump using synthetic jet actuators," *AIP Advances*, Vol. 12, No. 9, 2022. https://doi.org/10.1063/5.0099926, URL https://doi.org/10.1063/5.0099926.

[4] Kang, Y., bing Luo, Z., Deng, X., Cheng, P., Peng, C., He, W., and xun Xia, Z., "Numerical study of a liquid cooling device based on dual synthetic jets actuator," *Applied Thermal Engineering*, Vol. 219, No. PD, 2023, p. 119691. https://doi.org/10.1016/j.applthermaleng.2022.119691, URL https://doi.org/10.1016/j.applthermaleng.2022.119691.

[5] Mooney, H., Brandt, J., Lacy, D., and Whalen, E., "AFC-Enabled Vertical Tail System Integration Study," Tech. Rep. March 2014, NASA, 2014.

[6] Lin, J. C., Andino, M. Y., Alexander, M. G., Whalen, E. A., Spoor, M. A., Tran, J. T., and Wygnanski, I. J., "An Overview of Active Flow Control Enhanced Vertical Tail Technology Development," *54th AIAA Aerospace Sciences Meeting*, 2016. https://doi.org/10.2514/6.2016-0056, URL http://arc.aiaa.org/doi/10.2514/6.2016-0056.

[7] Gallas, Q., Mathew, J., Kasyap, A., Holman, R., Nishida, T., Carroll, B., Sheplak, M., and Cattafesta, L., "Lumped Element Modeling of Piezoelectric-Driven Synthetic Jet Actuators," *AIAA Journal*, Vol. 41, No. 2, 2003, pp. 240–247. https://doi.org/10.2514/2.1936, URL http://arc.aiaa.org/doi/10.2514/2.1936.

[8] Sharma, R. N., "Some Insights into Synthetic Jet Actuation From Analytical Modelling," *16th Australasian Fluid Mechanics Conference*, Gold Coast, 2007, pp. 1242–1248. URL http://espace.library.uq.edu.au/view/UQ:120918%5Cnhttp://espace.library.uq.edu.au/eserv/UQ:120918/Sharma_afmc_16_07.pdf.

[9] Gomes, L., and Crowther, W., "Towards a practical piezoceramic diaphragm based synthetic jet actuator for high subsonic applications - effect of chamber and orifice depth on actuator peak velocity," *3rd AIAA Flow Control Conference*, Reno, NV, 2006. https://doi.org/10.2514/6.2006-2859, URL http://arc.aiaa.org/doi/10.2514/6.2006-2859.

[10] Lindstrom, A., and Amitay, M., "Effect of orifice geometry on synthetic jet evolution," *AIAA Journal*, Vol. 57, No. 7, 2019, pp. 2783–2794. https://doi.org/10.2514/1.J058135, URL https://doi.org/10.2514/1.J058135.

[11] Jabbal, M., Liddle, S., Potts, J., and Crowther, W., "Development of design methodology for a synthetic jet actuator array for flow separation control applications," *Proceedings of the Institution of Mechanical Engineers, Part G: Journal of Aerospace Engineering*, Vol. 227, No. 1, 2013, pp. 110–124. https://doi.org/10.1177/0954410011428256.

[12] Weigel, P., Schüller, M., Gratias, A., Lipowski, M., ter Meer, T., and Bardet, M., "Design of a synthetic jet actuator for flow separation control," *CEAS Aeronautical Journal*, Vol. 11, No. 4, 2020, pp. 813–821. https://doi.org/10.1007/s13272-020-00479-2, URL https://doi.org/10.1007/s13272-020-00479-2.

[13] Rathay, N. W., Boucher, M. J., Amitay, M., and Whalen, E., "Performance enhancement of a vertical stabilizer using synthetic jet actuators: Non-zero sideslip," *6th AIAA Flow Control Conference 2012*, Nashville, Tennessee, 2012, pp. 1–15. https://doi.org/10.2514/6.2012-71.

[14] Rathay, N., Boucher, M., Amitay, M., and Whalen, E., "Parametric study of synthetic-jet-based control for performance enhancement of a vertical tail," *AIAA Journal*, Vol. 52, No. 11, 2014, pp. 2440–2454. https://doi.org/10.2514/1.J052887.

[15] Van Buren, T., Whalen, E., and Amitay, M., "Achieving a High-Speed and Momentum Synthetic Jet Actuator," *Journal of Aerospace Engineering*, Vol. 29, No. 2, 2016, p. 04015040. https://doi.org/10.1061/(ASCE)AS.1943-5525.0000530, URL http://ascelibrary.org/doi/10.1061/%28ASCE%29AS.1943-5525.0000530.

[16] Aigouy, G., Barnique, A., Claeyssen, F., Ternoy, F., Eglinger, E., Dandois, J., Gallas, Q., Schüller, M., Schüller, S., and Kaulfersch, E., "SYNJET3C Improvement of Synthetic Jet Actuator Technology for High Efficiency SJA System Modelling in fre- quency domain," 2022, pp. 76–80.

[17] Crowther, W. J., and Gomes, L. T., "An evaluation of the mass and power scaling of synthetic jet actuator flow control technology for civil transport aircraft applications," *Proceedings of the Institution of Mechanical Engineers. Part I: Journal of Systems and Control Engineering*, Vol. 222, No. 5, 2008, pp. 357–372. https://doi.org/10.1243/09596518JSCE519.

[18] Jabbal, M., and Kykkotis, S., "Towards the Noise Reduction of Piezoelectrical-Driven Synthetic Jet Actuators," *32nd AIAA Applied Aerodynamics Conference*, Vol. 266, No. June, 2014, pp. 273–284. https://doi.org/10.2514/6.2014-2975, URL http://linkinghub.elsevier.com/retrieve/pii/S0924424717301929%0Ahttp://arc.aiaa.org/doi/10.2514/6.2014-2975.

[19] Feero, M. A., Lavoie, P., and Sullivan, P. E., "Influence of cavity shape on synthetic jet performance," *Sensors and Actuators, A: Physical*, Vol. 223, 2015, pp. 1–10. https://doi.org/10.1016/j.sna.2014.12.004, URL http://dx.doi.org/10.1016/j.sna.2014.12.004.

[20] Smyk, E., Wawrzyniak, S., and Peszyński, K., "Synthetic jet actuator with two opposite diaphragms," *Mechanics and Mechanical Engineering*, Vol. 24, No. 1, 2020, pp. 17–25. https://doi.org/10.2478/mme-2020-0004.

[21] Rusovici, R., and Lesieutre, G. A., "Design of a single-crystal piezoceramic-driven synthetic jet actuator," *Smart Structures and Materials 2004: Smart Structures and Integrated Systems*, Vol. 5390, No. July 2004, 2004, p. 276. https://doi.org/10.1117/12.539576.

[22] Lam, K. H., Chan, H. L., Luo, H. S., Yin, Q. R., and Yin, Z. W., "Piezoelectrically actuated ejector using PMN-PT single crystal," *Sensors and Actuators, A: Physical*, Vol. 121, No. 1, 2005, pp. 197–202. https://doi.org/10.1016/j.sna.2005.01.003.

[23] Chiatto, M., Palumbo, A., and de Luca, L., "Design approach to predict synthetic jet formation and resonance amplifications," *Experimental Thermal and Fluid Science*, Vol. 107, No. May, 2019, pp. 79–87. https://doi.org/10.1016/j.expthermflusci.2019.05.013, URL https://doi.org/10.1016/j.expthermflusci.2019.05.013.

[24] de Luca, L., Girfoglio, M., and Coppola, G., "Modeling and Experimental Validation of the Frequency Response of Synthetic Jet Actuators," *AIAA Journal*, Vol. 52, No. 8, 2014, pp. 1733–1748. https://doi.org/10.2514/1.J052674, URL http://arc.aiaa.org/doi/10.2514/1.J052674.

[25] Van Buren, T., Whalen, E., and Amitay, M., "Synthetic Jet Actuator Cavity Acoustics: Helmholtz Versus Quarter-Wave Resonance," *Journal of Vibration and Acoustics*, Vol. 137, No. 5, 2015, p. 054501. https://doi.org/10.1115/1.4030216, URL http://vibrationacoustics.asmedigitalcollection.asme.org/article.aspx?doi=10.1115/1.4030216.

[26] Blevins, R. D., *Formulas for natural frequency and mode shape*, 6th ed., Van Nostrand Reinhold Co., New York, 1979. https://doi.org/10.1115/1.3153712.

[27] Prasad, S. A., Gallas, Q., Horowitz, S. B., Homeijer, B. D., Sankar, B. V., Cattafesta, L. N., and Sheplak, M., "Analytical Electroacoustic Model of a Piezoelectric Composite Circular Plate," *AIAA Journal*, Vol. 44, No. 10, 2006, pp. 2311–2318. https://doi.org/10.2514/1.19855, URL http://arc.aiaa.org/doi/10.2514/1.19855.

[28] Yu, T., Lesieutre, G. A., Griffin, S. F., and Sassoon, A., "Bimorph-driven synthetic jet actuators optimized for various piezoelectric materials using a low-order coupled electro-elastic-acoustic model," , No. January, 2019. https://doi.org/10.2514/6.2019-1353.

[29] Waqar, S., Wang, L., and John, S., *Piezoelectric energy harvesting from intelligent textiles*, Elsevier Ltd., 2015. https://doi.org/10.1016/B978-0-08-100201-8.00010-2, URL http://dx.doi.org/10.1016/B978-0-08-100201-8.00010-2.

[30] Jiang, X., Tang, F., Wang, J. T., and Chen, T., "Growth and properties of PMN-PT single crystals," *Physica C*, Vol. 365, 2001, pp. 678–683.

[31] Jabbal, M., and Jeyalingam, J., "Towards the noise reduction of piezoelectrical-driven synthetic jet actuators," *Sensors and Actuators, A: Physical*, Vol. 266, 2017, pp. 273–284. https://doi.org/10.1016/j.sna.2017.09.036, URL https://doi.org/10.1016/j.sna.2017.09.036.

[32] Mane, P., Mossi, K., Rostami, A., Bryant, R., and Castro, N., "Piezoelectric actuators as synthetic jets: Cavity dimension effects," *Journal of Intelligent Material Systems and Structures*, Vol. 18, No. 11, 2007, pp. 1175–1190. https://doi.org/10.1177/1045389X06075658.

[33] Rizzetta, D. P., Visbal, M. R., and Stanek, M. J., "Numerical Investigation of Synthetic-Jet Flowfields," *AIAA Journal*, Vol. 37, No. 8, 1999, pp. 919–927. https://doi.org/10.2514/2.811, URL http://arc.aiaa.org/doi/10.2514/2.811.

[34] Tang, H., and Zhong, S., "Lumped element modelling of synthetic jet actuators," *Aerospace Science and Technology*, Vol. 13, No. 6, 2009, pp. 331–339. https://doi.org/10.1016/j.ast.2009.06.004, URL http://dx.doi.org/10.1016/j.ast.2009.06.004.

[35] Tang, H., Zhong, S., Jabbal, M., Garcillan, L., Guo, F., Wood, N., and Warsop, C., "Towards the design of synthetic-jet actuators for full-scale flight conditions : Part 2: Low-dimensional performance prediction models and actuator design method," *Flow, Turbulence and Combustion*, Vol. 78, No. 3-4, 2007, pp. 309–329. https://doi.org/10.1007/s10494-006-9061-3.

[36] Oshana, R., "Overview of Digital Signal Processing Algorithms," *DSP Software Development Techniques for Embedded and Real-Time Systems*, 2006, pp. 59–121. https://doi.org/10.1016/B978-075067759-2/50006-5.

[37] Gallas, Q., Holman, R., Nishida, T., Carroll, B., Sheplak, M., and Cattafesta, L., "Lumped Element Modeling of Piezoelectric-Driven Synthetic Jet Actuators," *AIAA Journal*, Vol. 41, No. 2, 2003, pp. 240–247. https://doi.org/10.2514/2.1936, URL http://arc.aiaa.org/doi/10.2514/2.1936.

[38] Persoons, T., "General reduced-order model to design and operate synthetic jet actuators," *AIAA Journal*, Vol. 50, No. 4, 2012, pp. 916–927. https://doi.org/10.2514/1.J051381.

[39] Yu, T., "Parametric and topology optimization for multidisciplinary deisgn using a decomposition method to address nonlinear boundary conditions," Ph.D. thesis, The Pennsylvania State University, 2022. URL https://etda.libraries.psu.edu/catalog/20424tuy127.

[40] van Buren, T., Whalen, E., and Amitay, M., "Interaction between a vortex generator and a synthetic jet in a crossflow," *Physics of Fluids*, Vol. 27, No. 10, 2015. https://doi.org/10.1063/1.4932359.